

Vulnerability-Aware Spatio-Temporal Learning for Generalizable and Interpretable Deepfake Video Detection

Dat NGUYEN[♠], Marcella ASTRID[♠], Anis KACEM[♠], Enjie GHORBEL^{♠,✗}, Djamila AOUADA[♠]
 CVI², SnT, University of Luxembourg[♠]
 Cristal Laboratory, National School of Computer Sciences, University of Manouba[✗]
 {dat.nguyen, marcella.astrid, anis.kacem, enjie.ghorbel, djamila.aouada}@uni.lu

Abstract

Detecting deepfake videos is highly challenging due to the complex intertwined spatial and temporal artifacts in forged sequences. Most recent approaches rely on binary classifiers trained on both real and fake data. However, such methods may struggle to focus on important artifacts, which can hinder their generalization capability. Additionally, these models often lack interpretability, making it difficult to understand how predictions are made. To address these issues, we propose *FakeSTormer*, offering two key contributions. First, we introduce a multi-task learning framework with additional spatial and temporal branches that enable the model to focus on subtle spatio-temporal artifacts. These branches also provide interpretability by highlighting video regions that may contain artifacts. Second, we propose a video-level data synthesis algorithm that generates pseudo-fake videos with subtle artifacts, providing the model with high-quality samples and ground truth data for our spatial and temporal branches. Extensive experiments on several challenging benchmarks demonstrate the competitiveness of our approach compared to recent state-of-the-art methods. The code is available at <https://github.com/10Ring/FakeSTormer>.

1. Introduction

With the advances in generative modeling, deepfake videos have become alarmingly realistic. Despite their interest in several applications such as entertainment and education, this type of technology also raises societal concerns [5, 44, 52]. There is therefore an urgency for developing effective deepfake detection methods.

In the literature, several deepfake detection techniques aim to model spatial artifacts by treating each frame independently [3, 6, 7, 15, 32, 39, 41, 42, 45, 47, 64]. While this is reasonable when dealing with frame-level generation methods [31, 50, 67], it becomes less adequate in the

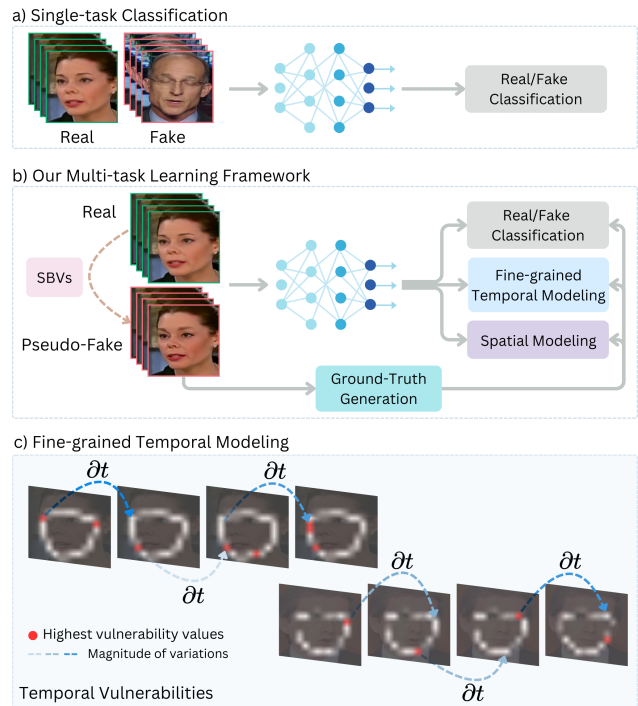


Figure 1. a) Traditional video-based methods [20, 22, 24, 55, 56, 60, 62, 65] versus b) the proposed multi-task learning framework; c) Visualization of the temporal vulnerabilities. Note that only some temporal locations are shown.

presence of video-level manipulation techniques [1, 19, 57], where temporal and spatial artifacts are *intertwined*.

For that reason, researchers have started investigating video deepfake detection methods that are capable of modeling spatio-temporal artifacts [20, 22, 24, 55, 60, 62, 65]. Those methods mainly rely on a deep neural network formed by a single binary classification branch that is trained using a fixed dataset with real and fake data (see Figure 1-a). As a result, they suffer from two main limitations, namely: (1) **The lack of generalizability** - As highlighted

in [32, 39, 42, 47], models trained with a standalone binary classifier tend to overfit the type of deepfakes they are trained on, resulting in poor generalization to unseen manipulations. To address this issue, multi-task learning and data synthesis strategies have demonstrated their relevance in image-based deepfake detection [6, 32, 42, 47, 63]. Nevertheless, such mechanisms have been disregarded in the field of video-level deepfake detection. (2) **The lack of interpretability** - As discussed in [18], binary outputs are opaque and difficult to interpret, despite the importance of explaining the decision of deepfake detectors. It has been shown in image-based deepfake detection that adding auxiliary non-binary branches can help in providing more explainable outputs [6, 32, 38, 42]. However, as mentioned earlier, multi-task learning strategies remain underexplored in the field of video-based deepfake detection.

A data synthesis strategy has been explored for video deepfake detection. STC [33] uses a Spatio-Temporal Generator (STG) to create pseudo-fake data from real data, improving model generalizability by blending two sequences, one of which has its frames shuffled in the temporal domain. However, this frame shuffling can introduce noticeable temporal artifacts (illustrations are shown in the supplementary materials). As demonstrated in image deepfake detection [47], pseudo-fake data with subtler artifacts improves generalization. To address this, we propose a method that generates subtler temporal artifacts. Additionally, our multi-task approach provides interpretability for the model’s output.

In this paper, to build a model that is both generalizable and interpretable, we propose utilizing a multi-branch network that trains on synthesized data and integrates learning objectives specifically targeting both spatial and subtle temporal artifacts. As shown in Figure 1-b, a novel multi-task learning framework, termed FakeSTormer is introduced and formed by two auxiliary parallel branches in addition to the standard classification head, namely: (1) **a regression temporal branch** that aims at predicting the vulnerability-prone temporal locations. It has been demonstrated that regressing spatial vulnerabilities in specific points [42] or patches [41] can help improve the generalizability of a deepfake detector model. We refer to the definitions given in [41, 42] which describe: “*vulnerable patches/points as the patches/points that are the most likely to embed blending artifacts*”. To generalize this concept to the temporal domain, we propose locating temporal high changes in spatial vulnerable patches (see Figure 1-c). (2) **a spatial branch** to ensure a balance between the spatial and the temporal domains. In fact, detecting spatial artifacts in addition to temporal ones is crucial [55, 62]. For that purpose, we propose predicting frame-wise spatial vulnerabilities.

To create ground truths for these two branches, we introduce a video-level data synthesis algorithm, called “Self-

Blended Videos (SBVs)”, inspired by “Self-Blended Images (SBIs) [47]. Our experiments demonstrate that simply training a baseline classification model on SBVs enables achieving on par performance w.r.t. state-of-the-art (SOTA), highlighting the effectiveness of SBVs. Finally, for enhancing spatial and temporal modeling, we revisit the TimeSformer [2] architecture that we use as our backbone. In particular, we leverage TimeSformer’s decomposed temporal and spatial attention on embedded patches, appending classification tokens for each frame and for each patch across frames, rather than a single token for the entire video. These classification tokens are then used within the spatial and classification heads, while the embedded patches are used within the temporal head. Extensive experiments on several well-known deepfake detection benchmarks show that our method is competitive against the existing SOTA approaches in terms of generalization capabilities, while providing more interpretable outputs through the proposed auxiliary branches.

Contributions. In summary, we propose in this paper:

- A novel multi-task learning framework for video-based deepfake detection, enhancing both generalization and interpretability aspects.
- Two auxiliary branches that capture both temporal and spatial vulnerabilities, that are fined-grained.
- A video-level data synthesis technique called SBVs that generates high-quality deepfakes and is supported by a vulnerability-driven cutout augmentation strategy to avoid overfitting specific artifact-prone regions.
- A revisited version of the TimeSformer [2], specifically tailored for the proposed video-based deepfake detector.
- Extensive experiments and analyses conducted on several challenging datasets.

Paper organization. Section 2 reviews related work on video deepfake detection. Section 3 describes the proposed FakeSTormer method. Section 4 presents experiments and results. Finally, Section 5 concludes with future work.

2. Related Work: Video-based Deepfake Detection

Using a naive spatio-temporal binary classifier for deepfake video detection can lead to overfitting on obvious artifacts, reducing generalization [55, 65]. To address this, FTCN [65] uses a fully temporal convolution network, reducing the spatial kernel size to minimize focus on spatial artifacts. LipForensics [24] focuses on the mouth region, and spatiotemporal dropout [60] removes parts of input frames across both spatial and temporal domains. AltFreezing [55] convolution layers into spatial and temporal ones, but it can fail to model long-term dependencies. ISTVT [62] uses a Vision Transformer with self-attention (SA) for longer-range correlations, splitting SA into spatial

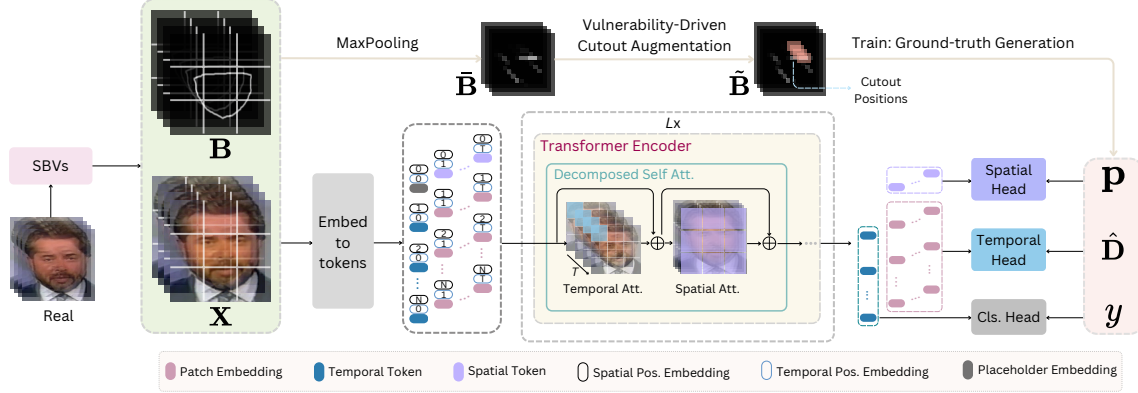


Figure 2. **Overview of the proposed framework.** Our multi-task learning framework, FakeSTormer consists of three branches, i.e., the temporal branch h , the spatial branch g , and the standard classification branch f . Those branches are specially designed to facilitate disentanglement learning of spatial-temporal features. The ground-truth data to train the framework are generated based on our proposed video-level data synthesis algorithm coupled with a vulnerability-driven Cutout strategy.

and temporal. Additionally, [9] decomposes features into spatial and temporal components. Differently, TALL [56] employs an image-level deepfake detector by converting video frames into a thumbnail layout.

While promising, the aforementioned methods rely on training binary classifiers with both real and fake data, which can lead to overfitting on fake data artifacts. Training only on real data, as suggested in image-based deepfake detection [6, 32, 42], can improve generalization. Using only real data, the recent STC [33] method generates pseudo-fake samples using time-shuffling, but this creates obvious temporal artifacts. Inspired by image-based methods [47], we propose a pseudo-fake generation technique that creates subtler artifacts, improving generalization. Additionally, our approach incorporates a multi-task setup, which enhances both model performance and interpretability.

3. Methodology

Let $\mathcal{V} \triangleq \cup_{i=1}^N \{(\mathbf{X}_i, y_i)\}$ be a training dataset formed by N videos, where \mathbf{X}_i denotes the i^{th} video sample and y_i its associated label indicating whether the clip is real ($y_i = 0$) or fake ($y_i = 1$). Traditional methods [20, 22, 24, 55, 56, 60, 62, 65] aim to learn jointly a feature extractor $\Phi : \mathcal{V} \mapsto \mathcal{F}$ and a binary classifier $f : \mathcal{F} \rightarrow \{0, 1\}$ by minimizing the standard binary cross-entropy (BCE) loss $\mathcal{L}_{BCE}(f(\Phi(\mathbf{X}_i)), y_i)$ using the entire training set \mathcal{V} , with \mathcal{F} being the learned feature space. As highlighted in Section 1, such a strategy might lead to poor generalization capabilities to unseen generation methods [32, 39, 42, 47] while providing only binary outputs that are not interpretable.

To tackle these issues, inspired by the literature on image-level deepfake detection [6, 15, 32, 42, 63], we introduce a novel multi-task learning framework called FakeSTormer that only relies on the real data subset denoted as $\mathcal{V}^r \subset \mathcal{V}$. Specifically, in addition to the binary clas-

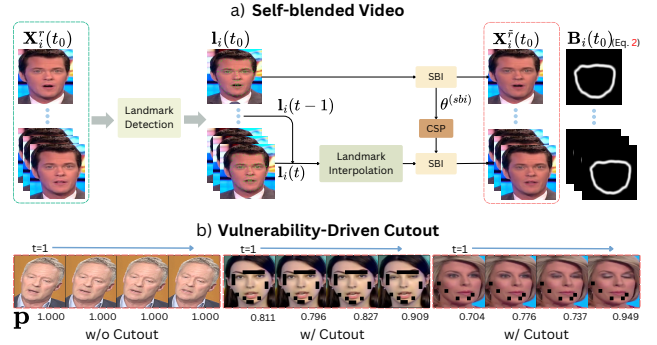


Figure 3. a) **Overview of generating a self-blended video.** It contains two main components including a landmark interpolation module and the consistent utilization of synthesized parameters (CSP). b) **Examples of pseudo-fake videos.** (with(w/) and without(w/o) vulnerability-driven Cutout and their corresponding soft labels. We apply the Cutout data augmentation at the same spatial locations throughout video frames.

sifier f , our framework includes two additional branches $h : \mathcal{F} \rightarrow \mathcal{H}$ and $g : \mathcal{F} \rightarrow \mathcal{G}$ that aim at triggering the learning of localized temporal and spatial artifact-prone features, respectively, through relevant auxiliary tasks. Note that \mathcal{G} and \mathcal{H} denote respectively the output spaces of h and g . The proposed branches are depicted further in Section 3.2. To provide ground truth to those branches and at the same time avoid overfitting to specific manipulations, we apply to each video belonging to \mathcal{V}^r a data synthesis method described in Section 3.1, resulting in a pseudo-fake subset denoted as $\mathcal{V}^{\bar{r}}$. Hence, our framework is trained using $\tilde{\mathcal{V}} \triangleq \{\mathcal{V}^r \cup \mathcal{V}^{\bar{r}}\}$.

3.1. Video-Level Data Synthesis and Augmentation

Self-Blended Videos. Blending-based data synthesis methods have demonstrated great performance in image-based deepfake detection [6, 7, 32, 41, 42, 47, 63]. In fact, as the blending step is common to different manipulation

types, they contribute to the improvement of the generalization aspect in deepfake detection [32, 42]. Nevertheless, such an approach has been overlooked in the context of video-based deepfake detection. Hence, we propose to extend blending-based data synthesis to the video level. In particular, we revisit SBI [47] given its ability to produce high-quality pseudo-fake images that have contributed to improving the generalization capabilities of deepfake detectors. The proposed data synthesis approach termed Self-Blended Videos (SBVs) is constituted of two main components, *i.e.*, a Landmark Interpolation module followed by a Consistent Synthesized Parameters (CSP) module for preserving the temporal coherence of synthesized videos, which is essential for producing high-quality synthesized videos. Specifically, given a real video $\mathbf{X}_i^r \in \mathcal{V}^r$ formed by T consecutive frames, we start by extracting a set of 2D landmarks $\mathbf{L}_i(t) = \{\mathbf{l}_{ij}(t)\}_{1 \leq j \leq n}$ at each instant t from $\mathbf{X}_i^r(t)$, where n refers to the number of landmarks and $\{\mathbf{l}_{ij}(t)\} \in \mathbb{R}^2$. Then, we apply SBI to the 1st video frame denoted as $\mathbf{X}_i^r(t_0)$ to obtain a pseudo-fake image, *i.e.*, $\mathbf{X}_i^{\tilde{r}}(t_0)$ and a blending mask $\mathbf{M}_i(t_0)$. All related blending parameters $\theta^{(sbi)}$ (e.g., ConvexHull type, Mask deformation kernels, blending ratio, etc.) are then conserved for synthesizing the remaining video frames. However, using those parameters solely cannot guarantee the temporal consistency of pseudo-fake videos since the geometry of landmarks can significantly vary over time. To mitigate the issue, we propose to re-interpolate each landmark $\mathbf{l}_i(t)$ based on $\mathbf{l}_i(t-1)$ for $t > t_0$ as follows,

$$\mathbf{l}_i(t) = \begin{cases} \mathbf{l}_i(t-1) + \frac{\mathbf{l}_i(t) - \mathbf{l}_i(t-1)}{\text{round}(d/\bar{d})}, & \text{if } d > \tau \\ \mathbf{l}_i(t), & \text{otherwise,} \end{cases} \quad (1)$$

where $d = \|\mathbf{l}_i(t) - \mathbf{l}_i(t-1)\|_2/n$

where d represents the normalized distance between the position of a given landmark at the instants t and $t-1$, τ is a constant threshold for determining when to interpolate (interpolation intervenes only in the presence of drastic changes), and \bar{d} is empirically chosen. Overall, a higher d value will push the updated point to move closer to the previous landmark position $\mathbf{l}_i(t-1)$, hence contributing to smooth the landmark position over time. However, excessive smoothing can be disadvantageous, as it can discard temporal artifacts. To address this, we use a round operator to incorporate slight errors. Hence, the proposed SBV data synthesis produces high-quality pseudo-fake videos incorporating subtle temporal artifacts.

As a result, we obtain the pseudo-fake video $\mathbf{X}_i^{\tilde{r}} \in \mathcal{V}^{\tilde{r}}$ and its blending mask sequence $\mathbf{M}_i \in \mathbb{R}^{T \times H \times W}$, with H and W being the image height and width, respectively. An illustration of SBVs is given in Figure 3. Additional samples as well as the detailed algorithm are provided in supplementary materials. It is important to note that despite

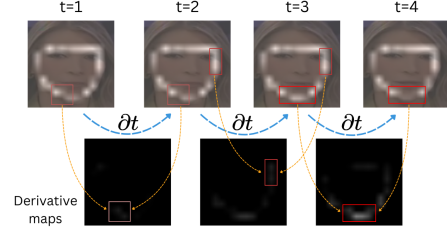


Figure 4. **Extraction of temporal vulnerabilities.** We compute derivatives of the spatial vulnerabilities over time.

being simple, SBVs is generic and applicable to any existing video-level deepfake detection approach.

Vulnerability-Driven Cutout Augmentation. Previous works [53, 66] have demonstrated that deep learning methods are often impacted by overfitting. Deepfake detectors might even be more sensitive to this phenomenon as deepfakes are typically characterized by localized artifacts [42]. One solution to regularize training is data augmentation. As such, we propose in addition to SBVs, a novel Cutout data augmentation driven by vulnerable patches, *i.e.*, image patches that are prone to blending artifacts [41]. We posit that by masking the most vulnerable regions, overfitting risks will be reduced, as the model will be pushed to learn from other areas. This masking strategy has already been explored in other computer vision fields such as Classification [8, 12], Object Detection [21] demonstrating great potential.

Specifically, similar to [32], we create a set of blending boundaries \mathbf{B} using a randomly generated blending mask \mathbf{M} as follows,

$$\mathbf{B} = (\mathbf{1} - \mathbf{M}) * \mathbf{M} * 4, \mathbf{B} \in \mathbb{R}^{T \times H \times W}, \quad (2)$$

with $*$ being the element-wise multiplication and $\mathbf{1}$ an all-one matrix. Inspired by [41], vulnerability values are then quantified at the patch level in a non-overlapping manner by applying a MaxPooling function as follows,

$$\bar{\mathbf{B}} = \text{MaxPooling}(\mathbf{B}), \bar{\mathbf{B}} \in \mathbb{R}^{T \times \sqrt{N} \times \sqrt{N}}, \quad (3)$$

where N indicates the number of patches.

After that, we define a threshold τ_{cutout} that is randomly selected from the range $(0.5, 1.0]$. We use the latter to define the set of patches to be masked $\mathcal{P} = \{(l, m) \mid \bar{\mathbf{B}}_{l,m}(t_0) > \tau_{cutout}\}$ within the first frame. The set \mathcal{P} is then used to mask out patches at those locations not only in the first frame but also in the entire video to enforce temporal consistency that is crucial for generating high-quality pseudo-fakes. After masking those patches over time, we finally obtain the masked blending boundary denoted as $\bar{\mathbf{B}}$. This results in masking the most vulnerable regions, *i.e.*, the regions that are the most likely to include

blending artifacts. Figure 3-b shows some examples of the proposed cutout augmentation.

3.2. FakeSTormer

Our multi-task framework called FakeSTormer is inspired by [41, 42], where auxiliary branches are designed to push the feature extractor to focus on vulnerabilities. As discussed earlier, the vulnerability is defined in [41, 42] as the pixel/patches that are the most likely to be impacted by blending artifacts. This strategy is therefore claimed to allow the detection of subtle artifacts that are generic across different types of manipulations. While such a vulnerability-driven approach has shown very promising results [41, 42], it does not take into account the temporal nature of videos. Therefore, in addition to spatial vulnerabilities, we argue that there is a need to model temporal vulnerabilities, which we define as significant temporal changes in the blending boundary. Specifically, we introduce two additional branches, namely a temporal head h and a spatial one g . The branch h predicts the derivatives of the blending boundary over time which can reflect high changes, typically characterizing temporal artifacts. Moreover, we suggest the use of a spatial branch g which enables predicting soft labels representing the forgery intensity encoded in each frame, computed from vulnerability information. The proposed framework relies on the TimeSformer backbone [2], which we revisit for better modeling spatial and temporal information.

Herein, we first describe the proposed revisited TimeSformer-based feature extractor Φ in Section 3.2.1. We then detail the two additional temporal and spatial heads in Section 3.2.2 and Section 3.2.3, respectively. Finally, we give the overall training details in Section 3.2.4.

3.2.1. Backbone: Revisited TimeSformer

We choose TimeSformer [2] as our feature extractor given its ability to effectively capture separate long-range temporal information and spatial features. In TimeSformer, a video input $\mathbf{X} \in \mathbb{R}^{C \times T \times H \times W}$ results in an embedding matrix input $\mathbf{Z}^0 \in \mathbb{R}^{T \times N \times D}$. A global class token \mathbf{z}_{cls} attends all patches and is then used for classification. This mechanism implicitly captures mixed spatio-temporal features, which might lead to overfitting one type of artifact. We revisit it slightly in order to decouple the spatial and temporal information by considering two sorts of additional tokens (one spatial and one temporal).

For that purpose, we attach in each dimension of \mathbf{Z}^0 , a spatial token $\mathbf{z}_s^0 \in \mathbb{R}^D$ and a temporal token $\mathbf{z}_t^0 \in \mathbb{R}^D$, respectively. These tokens will independently interact only with patch embeddings belonging to their dimension axis by leveraging the decomposed SA [2]. This mechanism not only facilitates the disentanglement learning process of spatio-temporal features but is also beneficial to optimize the computational complexity of $\mathcal{O}(T^2 + N^2)$ as compared

to $\mathcal{O}(T^2 \cdot N^2)$ in vanilla SA. Those tokens will be then fed into L ($L = 12$ as default) transformer encoder blocks, as described in Figure 2. Formally, the feature extraction process can be summarized as follows,

$$[\mathbf{Z}^L, \mathbf{z}_s^L, \mathbf{z}_t^L] = \Phi(\mathbf{X}), \quad (4)$$

where \mathbf{Z}^L is the final patch embedding matrix, \mathbf{z}_s^L the resulting set of spatial tokens, and \mathbf{z}_t^L the resulting set of temporal tokens that will be respectively sent to the temporal head h , the spatial head g , and the classification head f . More details about the implementation of the proposed revisited TimeSformer are given in supplementary materials.

3.2.2. Temporal Head h

Ground Truths. Our temporal head h aims to model fine-grained temporal vulnerabilities in deepfake videos through a regression task. First, to generate ground truth data for the branch h , we hypothesize that temporal high-changes in the blending boundary can reflect the presence of temporal artifacts (see Figure 4). To achieve this, we compute \mathbf{D} based on $\tilde{\mathbf{B}}$ such that:

$$\mathbf{D} = \frac{\partial \tilde{\mathbf{B}}}{\partial t}, \quad \mathbf{D} \in \mathbb{R}^{T \times \sqrt{N} \times \sqrt{N}}. \quad (5)$$

More details regarding the derivative calculation are provided in supplementary materials. To stabilize training, \mathbf{D} is standardized resulting in $\hat{\mathbf{D}} \in \mathbb{R}^{T \times \sqrt{N} \times \sqrt{N}}$. Experiments with different normalization strategies are reported in supplementary materials.

Architecture Design. In order to construct the regression head for predicting $\hat{\mathbf{D}}$, we take the patch embedding matrix \mathbf{Z}^L as input and process them to produce 3D features as follows,

$$\mathbf{F} = \text{Reshape}(\mathbf{Z}^L), \quad \mathbf{F} \in \mathbb{R}^{D \times T \times \sqrt{N} \times \sqrt{N}}. \quad (6)$$

To estimate temporal derivatives, we employ two 3D convolution blocks (3DCnvB) with 3-dimensional temporal kernels and 1-dimensional spatial kernels [65] as follows,

$$\tilde{\mathbf{D}} = h(\mathbf{F}) = 3\text{DCnvB}_{3 \times 1 \times 1}(3\text{DCnvB}_{3 \times 1 \times 1}(\mathbf{F})), \quad (7)$$

where $\tilde{\mathbf{D}} \in \mathbb{R}^{T \times \sqrt{N} \times \sqrt{N}}$. Each convolution block comprises a 3D convolution layer, followed by a BatchNorm and a GELU layer.

Objective Function. For training the temporal branch, we optimize the following Mean Square Error (MSE) loss,

$$\mathcal{L}_h = \frac{1}{T \times N} \|\hat{\mathbf{D}} - \tilde{\mathbf{D}}\|_2^2, \quad (8)$$

with $\|\cdot\|_2$ referring to the L_2 norm.

3.2.3. Spatial Head g

Ground Truths. To avoid overfitting one type of artifact, we enforce the model to explicitly predict soft labels representing the intensity level of spatial artifacts for each video frame. Note that, several works [4, 40, 48, 51, 61] have leveraged soft labels for training regularization. Given a pseudo-fake video $\mathbf{X} = (\mathbf{X}(t))_{t \in [[1, T]]}$ formed by T frames and $\tilde{\mathbf{B}} = (\tilde{\mathbf{B}}(t))_{t \in [[1, T]]}$ its associated cutout blending boundary, the ground truth for these soft labels is generated for each frame t as follows,

$$p(t) = \max_{l, m \in [[1, \sqrt{N}]]} (\tilde{\mathbf{B}}(t)), \quad (9)$$

resulting in the ground truth for training the spatial branch denoted as $\mathbf{p} = (p(t))_{t \in [[1, T]]}$. We note that $\mathbf{p} = \mathbf{1}^T$ if cutout is not applied and $\mathbf{p} = \mathbf{0}^T$ for a real video.

Architecture Design. To predict the proposed soft labels, a Multi-Layer Perceptron (MLP) is applied to the set of spatial tokens \mathbf{z}_s^L , as follows,

$$\tilde{\mathbf{p}} = g(\mathbf{z}_s^L) = \text{MLP}(\mathbf{z}_s^L), \quad \tilde{\mathbf{p}} \in \mathbb{R}^T. \quad (10)$$

Objective Function. To train the spatial branch, we optimize the following Binary Cross Entropy (BCE) loss similar to [51, 61],

$$\mathcal{L}_g = \text{BCE}(\tilde{\mathbf{p}}, \mathbf{p}). \quad (11)$$

3.2.4. Overall Training Objective

Finally, for the standard classification head f , we use the set of temporal tokens \mathbf{z}_t^L such that the predicted label \tilde{y} is given by,

$$\tilde{y} = f(\mathbf{z}_t^L) = \text{MLP}(\mathbf{z}_t^L). \quad (12)$$

The classification loss \mathcal{L}_c is then given by applying a BCE between the ground-truth label y and the predicted label \tilde{y} .

Overall, the network is trained by optimizing the following loss:

$$\mathcal{L} = \lambda_c \mathcal{L}_c + \lambda_h \mathcal{L}_h + \lambda_g \mathcal{L}_g, \quad (13)$$

where $\lambda_c, \lambda_h, \lambda_g$ are hyper-parameters to balance the training of the three branches.

4. Experiment

4.1. Settings

Datasets. We set up our datasets following several works [3, 9, 54–56, 58, 62, 65]. For both training and validation, we employ **FaceForensics++** (FF++) [45], which consists of four manipulation methods for the fake data (Deepfakes (DF) [10], FaceSwap (FS) [30], Face2Face (F2F) [50], and NeuralTextures (NT) [49]). It can be noted that, for training, we use only the real videos and generate pseudo-fake data using our synthesized method, SBVs.

| Method | Inter. | Training | | Test set AUC (%) | | | |
|--------------------------|--------|----------|-------------|------------------|-------------|-------------|-------------|
| | | Fake | CDF | DFD | DFDCP | DFDC | DFW |
| Xception [45] | × | ✓ | 73.7 | - | - | 70.9 | - |
| MATT [64] | × | ✓ | 68.3 | 92.9 | 63.0 | - | 65.7 |
| RECCE [3] | × | ✓ | 70.9 | <u>98.2</u> | - | - | 68.2 |
| SFDG [54] | × | ✓ | 75.8 | 88.0 | 73.6 | - | <u>69.3</u> |
| LSDA [59] | × | ✓ | 91.1 | - | <u>77.0</u> | - | - |
| STIL [22] | × | ✓ | 75.6 | - | - | - | - |
| LipForensics [24] | × | ✓ | 82.4 | - | - | <u>73.5</u> | - |
| RealForensics [25] | × | ✓ | 86.9 | 82.2 | 75.9 | - | - |
| FTCN [65] | × | ✓ | 86.9 | 94.4 | 74.0 | 71.0 | - |
| ISTVT [62] | × | ✓ | 84.1 | - | 74.2 | - | - |
| AltFreezing [55] | × | ✓ | 89.5 | 98.5 | - | - | - |
| Swin+TALL [56] | × | ✓ | 90.8 | - | 76.8 | - | - |
| StyleLatentFlows [9] | × | ✓ | 89.0 | 96.1 | - | - | - |
| FakeSTormer ($T = 4$) | ✓ | × | 92.4 | 98.5 | 90.0 | 74.6 | 74.2 |
| FakeSTormer ($T = 8$) | ✓ | × | 92.4 | 98.2 | 90.0 | 74.9 | 75.9 |
| FakeSTormer ($T = 16$) | ✓ | × | 92.8 | 98.6 | 90.2 | 75.1 | 75.3 |

Table 1. **Generalization to unseen datasets.** AUC (%) comparisons on multiple unseen datasets [13, 14, 16, 35, 68]. All detectors are trained on FF++ (c23). Results are directly extracted from the original papers and from [24, 42]. **Bold** and Underlined text respectively highlight the best and the second best performance, excluding the variants of our framework with $T = 8$ and $T = 16$. *Inter.* denotes interpretability.

| Method | Inter. | Training set | | Test set AUC (%) | |
|-------------------|--------|--------------|------|------------------|-------------|
| | | Real | Fake | CDF | DFDCP |
| Face X-ray [32] | ✓ | ✓ | ✓ | 79.5 | - |
| PCL+I2G [63] | × | ✓ | ✓ | 90.0 | 74.3 |
| SLADD [6] | ✓ | ✓ | ✓ | 79.7 | - |
| SBI [47] | × | ✓ | × | 93.2 | 86.2 |
| LAA-Net [42] | ✓ | ✓ | × | 95.4 | 86.9 |
| STC-Scratch [33] | × | ✓ | × | 83.4 | 86.8 |
| STC-Pretrain [33] | × | ✓ | × | <u>95.8</u> | 89.4 |
| ST-SBV [23] | × | ✓ | × | 90.3 | <u>91.2</u> |
| FakeSTormer | ✓ | ✓ | × | 96.5 | 94.1 |

Table 2. **Comparison with other data synthesis methods.** For fair comparison, we train our FakeSTormer on raw data of FF++ (c0) and test on CDF [35] and DFDCP [13].

| Method | Training set | | FF++ LQ (%) | |
|------------------|--------------|----|-------------|-------------|
| | Real | NT | DF | FS |
| Xception [45] | ✓ | ✓ | 58.7 | 51.7 |
| Face X-ray [32] | ✓ | ✓ | 57.1 | 51.0 |
| F3Net [43] | ✓ | ✓ | 58.3 | 51.9 |
| RFM [53] | ✓ | ✓ | 55.8 | 51.6 |
| SRM [36] | ✓ | ✓ | 55.5 | 52.9 |
| SLADD [6] | ✓ | ✓ | 62.8 | 56.8 |
| TALL-Swin [56] | ✓ | ✓ | 63.2 | 51.4 |
| ResNet3D* [26] | ✓ | ✓ | 66.8 | <u>60.6</u> |
| TimeSformer* [2] | ✓ | ✓ | <u>73.3</u> | 54.4 |
| Ours | ✓ | × | 85.3 | 62.1 |

Table 3. **Generalization on heavily compressed data (LQ).** AUC (%) comparisons on FF++ (LQ) [45] with a high compression level (c40). The results for comparison are directly extracted from [6, 37]. The symbol * denotes our implementation.

By default, the c23 version of FF++ is adopted, following recent literature [9, 55, 56, 62, 65]. For further validation, we also evaluate on the following datasets: **Celeb-DFv2** (CDF) [35], **DeepfakeDetection** (DFD) [16], **Deepfake Detection Challenge Preview** (DFDCP) [13], **Deepfake Detection Challenge** (DFDC) [14], and **WildDeepfake** (DFW) [68]. Further details on these datasets are provided in the supplementary material.

Data Pre-processing. Following the splitting conven-

| Method | Training set | | FF++ (%) |
|----------------------|--------------|------|-------------|
| | Real | Fake | |
| Xception [45] | ✓ | ✓ | 77.9 |
| Face X-ray [32] | ✓ | ✓ | 94.9 |
| LipForensics [24] | ✓ | ✓ | 97.1 |
| FTCN [65] | ✓ | ✓ | 98.3 |
| AltFreezing [55] | ✓ | ✓ | 98.6 |
| StyleLatentFlows [9] | ✓ | ✓ | 98.4 |
| Ours (HQ) | ✓ | × | 98.4 |
| Ours (Raw) | ✓ | × | 99.9 |

Table 4. **Generalization to unseen manipulations.** AUC (%) comparisons on FF++ [45]. The results for comparison are extracted from the original papers.

tion [45], we extract 256, 32, and 32 consecutive frames for training, validation, and testing, respectively. Facial regions are cropped using Face-RetinaNet [11] and resized to a fixed resolution of 224×224 . Additionally, we store 81 facial landmarks for each frame, extracted using Dlib [29]. Further details are provided in the supplementary materials.

Evaluation Metrics. For fair comparisons with SOTA methods, we use the widely adopted Area Under the Curve (AUC) metric at the video level [9, 24, 25, 55, 56, 62, 65].

Implementation Details. Our framework is initialized with pretrained MAE weights [27] and trained for 100 epochs using the SAM optimizer [17] with a weight decay of 10^{-4} and a batch size of 32. The learning rate starts at 5×10^{-4} for the first quarter of training and decays to 0 thereafter. The backbone is frozen for the first 5 epochs for warm-up, then all layers are unfrozen. Data augmentation includes ColorJittering at the video level and our proposed Cutout. Experiments are conducted on four NVIDIA A100 GPUs, with $\tau = 0.35$ and $\bar{d} = 0.2$ (Eq. (1)), and $T = 4$ frames in most experiments.

4.2. Comparison with State-of-the-art Methods

Generalization to Unseen Datasets. To assess the generalization capabilities of our method, we conduct evaluations using the challenging *cross-dataset* setup [3, 42, 54, 55, 65], validating on unseen datasets (i.e., datasets other than FF++). The results are detailed in Table 1 and Table 2.

As shown, our method achieves comparable results on DFD while surpassing SOTA methods on other datasets. Specifically, it significantly outperforms prior video deepfake detection techniques, including spatio-temporal learning-based methods like AltFreezing [55] and ISTVT [62], as well as various data synthesis approaches. Moreover, our method exhibits superior performance on the large-scale DFDC dataset and the challenging in-the-wild DFW dataset. These results further confirm the enhanced generalization ability of FakeSTormer compared to recent methods.

Generalization on Heavily Compressed Data. Following previous work [6, 37], we also evaluate FakeSTormer on heavily compressed (c40) FF++ data. In addition

| SBV | V-CutOut | g | h | Test set AUC (%) | | | | | Avg. |
|-----|----------|-----|-----|------------------|-------------|-------------|-------------|-------------|--------------------|
| | | | | CDF2 | DFD | DFDCP | DFDC | DFW | |
| × | × | × | × | 61.5 | 62.8 | 59.4 | 58.5 | 65.2 | 61.5 |
| ✓ | × | × | × | 90.7 | 95.7 | 87.9 | 72.2 | 70.9 | 83.5(↑22.0) |
| ✓ | ✓ | × | × | 91.1 | <u>96.0</u> | 87.6 | 72.6 | 71.0 | 83.7(↑22.2) |
| ✓ | ✓ | ✓ | × | 92.2 | 95.4 | <u>88.5</u> | <u>72.8</u> | <u>71.3</u> | 84.0(↑22.5) |
| ✓ | × | × | ✓ | 93.4 | 98.5 | <u>88.5</u> | <u>72.8</u> | 69.6 | 84.6(↑23.2) |
| ✓ | ✓ | ✓ | ✓ | <u>92.4</u> | 98.5 | 90.0 | 74.6 | 74.2 | 85.9(↑24.4) |

Table 5. **Ablation study of framework’s components.** Gray indicates the use of original fake data for training.

| CSP | Lmk Interpolation | Test set AUC (%) | | | | | Avg. |
|-----|-------------------|------------------|-------------|-------------|-------------|-------------|--------------------|
| | | CDF2 | DFD | DFDCP | DFDC | DFW | |
| × | × | 48.4 | 49.1 | 48.9 | 51.7 | 52.8 | 50.2 |
| ✓ | × | <u>84.1</u> | <u>89.2</u> | <u>86.1</u> | 69.5 | 65.5 | 78.9(↑28.7) |
| ✓ | ✓ | 90.7 | 95.7 | 87.9 | 72.2 | 70.9 | 83.5(↑33.3) |

Table 6. **Ablation study of SBVs’ components.** Performance analyses of different SBVs’ components using cross-evaluation on multiple datasets [13, 14, 16, 35, 68].

to comparing with several SOTA methods, we train ResNet3D [26], commonly used in deepfake video detection [9, 55, 65], and TimeFormer [2] on NT, then test on DF and FS. The comparison results are presented in Table 3. Our method achieves notably higher AUC scores than other methods across both testing subsets, highlighting its robust generalization capability under various data compression conditions.

Generalization to Unseen Manipulations. Table 4 compares our framework with SOTA methods on FF++. Other methods [9, 24, 55, 65] use a cross-manipulation setup, training on three forgery types and evaluating on the remaining one. In contrast, our approach trains only on real videos, treating all manipulations as unseen. Despite this, our method shows competitive performance with the others, even without being trained on specific forgery types.

Robustness to Unseen Perturbations. Deepfakes are widely shared on social media, where various perturbations can affect their appearance. Following [28], we evaluate FakeSTormer’s robustness across six unseen degradation types at five levels, comparing it with other augmented-based methods [32, 34, 42, 47]. Figure 5 shows AUC scores for each method on these perturbations, using models trained on FF++. Our results demonstrate that FakeSTormer outperforms prior methods on most distortions, with a slight drop compared to LAA-Net [42] for Change Saturation. Nonetheless, FakeSTormer achieves higher performance on average, especially at higher severity levels, highlighting its superior generalization and robustness. Detailed scores are in the supplementary materials.

4.3. Additional Discussions

Ablation Study of the FakeSTormer’s Components. We conduct ablation studies to assess the impact of each component in our framework, as shown in Table 5. Using TimeFormer trained on FF++ as the baseline, we experiment with different combinations of components: Self-Blended Videos (SBVs), Vulnerability-driven CutOut (V-

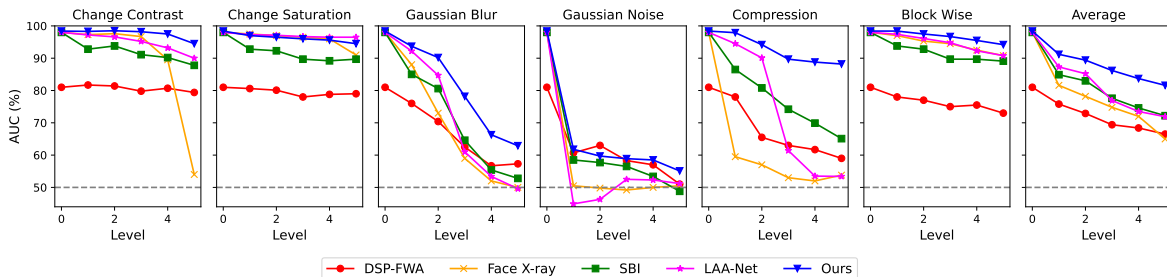


Figure 5. **Robustness to unseen perturbations.** AUC (%) under five different degradation levels for various types of perturbations [28] on FF++ [45]. “Average” denotes the mean across all corruptions at each level. Best viewed in color.

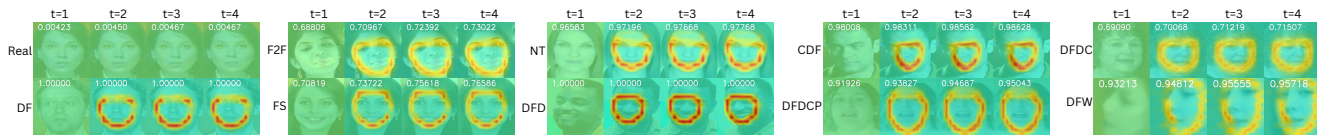


Figure 6. **Interpretability.** Visualization of spatial and temporal branch outputs on different unseen datasets. The number on each frame denotes the output of the spatial branch g , while the heatmap visualizes the output of the temporal branch h .

| λ_c | λ_h | λ_g | Test set AUC (%) | | | | | Avg. |
|-------------|-------------|-------------|------------------|-------------|-------------|-------------|-------------|-------------|
| | | | CDF2 | DFD | DFDCP | DFDC | DFW | |
| 0.9 | 1 | 0.1 | 89.5 | 91.0 | 93.2 | 71.5 | 74.7 | 84.0 |
| 0.9 | 10 | 0.1 | 92.5 | 95.7 | 86.8 | 71.7 | 72.7 | 83.9 |
| 0.9 | 100 | 0.1 | 91.6 | 98.0 | 87.3 | 73.6 | 70.6 | 84.2 |
| 0.8 | 100 | 0.2 | 92.4 | 98.5 | 90.0 | 74.6 | 74.2 | 85.9 |
| 0.5 | 100 | 0.5 | 92.4 | 98.0 | 88.1 | 74.5 | 72.1 | 85.0 |

Table 7. **Impacts of loss balancing factors.** AUC (%) comparisons of FakeSTormer trained with different values of λ_c , λ_h , and λ_g on cross-dataset setup, demonstrating robustness to varying hyperparameter settings.

CutOut), the spatial branch (g), and the temporal branch (h). Each component improves performance, with SBVs providing the most significant boost by generating high-quality pseudo-fake data that aids generalization to unseen datasets. **Ablation Study of the SBVs’ Components.** SBVs enhance SBI [47] with CSP and LmK Interpolation for robust pseudo-fake generation in video data. Table 6 shows that without these components, simply stacking frame-wise SBI fails to produce consistent temporal features, leading to overfitting on spatial artifacts and poor generalization.

Influence of Number of Frames. Increasing the number of frames T provides more fine-grained temporal information for FakeSTormer. In Table 1, we evaluate T values of 4, 8, and 16. Our results show consistent performance improvement with more frames, confirming our hypothesis. However, increasing T also incurs significant computational cost.

Impacts of Loss Balancing Factors. We introduce three hyperparameters, λ_c , λ_g , and λ_h in Eq (13) to balance the training among the three branches of our framework. In Table 7, we analyze the impact of these hyperparameters using various values. Our results show that the method is robust to a range of hyperparameter values, with the best performance achieved when λ_c , λ_g , and λ_h are set to 0.8,

0.2, and 100, respectively.

Interpretability. Our spatial and temporal branches output the intensity of the spatial artifacts in each video frame and the vulnerability change over time, respectively. These outputs provide valuable insights during testing, offering interpretability for our model. The spatial branch provides frame-level scores, while the temporal branch offers more fine-grained insights. As shown in Figure 6, the spatial branch output (denoted by the numbers on each frame) gives high values for fake data and low values for real data. For the temporal branch output, the heatmap shows the vulnerability change between each frame and the previous one. As observed, it primarily focuses around the blending boundaries.

5. Conclusion

This paper introduces a fine-grained approach for generalizable and interpretable deepfake video detection with two main contributions. First, we propose a multi-task learning framework that addresses both spatial and fine-grained temporal vulnerabilities in high-fidelity deepfake videos, incorporating a standard classification branch along with two new auxiliary branches (temporal and spatial). These proposed branches help the model focus on vulnerable regions and provide interpretable insights into how the network “sees” the data. Second, we present a high-quality pseudo-fake generation technique to improve model generalization by creating rich, generic spatio-temporal artifacts. Extensive experiments on challenging benchmarks demonstrate that FakeSTormer achieves competitive performance compared to SOTA methods while providing interpretability. Future work will investigate pretraining strategies for network initialization.

| Function | Test set AUC (%) | | | | | Avg. |
|--------------------------|------------------|-------------|-------------|-------------|-------------|-------------|
| | CDF2 | DFD | DFDCP | DFDC | DFW | |
| MinMax | 91.6 | <u>95.9</u> | <u>88.1</u> | 71.1 | 70.1 | 83.4 |
| Unnormalized 3D Gaussian | 92.5 | 91.8 | 86.4 | <u>72.4</u> | 76.3 | <u>83.9</u> |
| MeanStd | <u>92.4</u> | 98.5 | 90.0 | 74.6 | <u>74.2</u> | 85.9 |

Table 8. **Comparison of different normalization functions.** We consider three normalization functions, i.e., Standardization (MeanStd), MinMax, and Unnormalized 3D Gaussian. Among these, Standardization gives the best overall performance.

6. Appendix

6.1. Code Release

The code is provided as a part of the supplementary materials. The code is under license registration and will be publicly released with pretrained weights.

6.2. Details of the Ground-Truth Derivative

Calculation formula. To generate the ground truth data for the temporal branch h , we compute the derivative on $\tilde{\mathbf{B}} = (\tilde{\mathbf{B}}(t))_{t \in [[1, T]]}$ with respect to the temporal dimension. Specifically, we calculate the absolute value of the difference between two consecutive patch-level vulnerability values $\tilde{\mathbf{B}}(t)$ and $\tilde{\mathbf{B}}(t-1)$ with $t \geq 2$ such that,

$$\mathbf{D}(t) = \left| \tilde{\mathbf{B}}(t) - \tilde{\mathbf{B}}(t-1) \right|. \quad (14)$$

The process is iterated for every pair of consecutive frames of $(\tilde{\mathbf{B}}(t))_{t \in [[1, T]]}$ to obtain a derivative matrix $\mathbf{D} \in \mathbb{R}^{T \times \sqrt{N} \times \sqrt{N}}$. For $t = 1$, we insert a matrix $\mathbf{0}$, i.e., $\mathbf{D}(1) = \mathbf{0}$, indicating no temporal change at the first frame. **Normalization functions.** Employing a normalization function is important for stabilizing the training of our temporal branch h . Therefore, we consider three different normalization functions including Standardization (MeanStd), MinMax, and Unnormalized 3D Gaussian. Specifically, for the Standardization and MinMax, we respectively compute the $\text{std}(\mathbf{D})$ - $\text{mean}(\mathbf{D})$, and $\text{min}(\mathbf{D})$ - $\text{max}(\mathbf{D})$, while we follow the work of [41] to adapt an unnormalized Gaussian map from 2D to 3D for normalization. We report in Table. 8 cross-evaluation results on five datasets [13, 14, 16, 35, 68] with the use of the three investigated functions, using a model trained on FF++ [45]. It can be noted that the model is robust to various types of normalization functions with the best performance recorded for the Standardization approach.

6.3. SBVs: Pseudo-code and Visual Samples

Algorithm. To enhance the clarity and reproducibility of the SBVs generation process, we provide the overall algorithm in the form of pseudo-code, as detailed in Algorithm 1.

Visual Samples. To visually demonstrate the benefits of the Consistent Synthesized Parameters (CSP) and the Land-

Algorithm 1: Pseudo-code for SBVs Generation

Input: Real video $\mathbf{X}_i^r \in \mathcal{V}^r$ of size (C, T, H, W) , facial landmarks $\mathbf{L}_i \triangleq \cup_{t=1}^T \{\mathbf{l}_{ij}(t)\}_{1 \leq j \leq n}$ of size $(T, n, 2)$, a distance \bar{d} , a threshold τ

Output: Self-blended video $\mathbf{X}_i^{\tilde{r}} \in \mathcal{V}^{\tilde{r}}$ of size (C, T, H, W) , blending mask \mathbf{M}_i of size (T, H, W)

```

1 Initialize  $\theta^{(sbi)}$  as an empty dictionary
2 Initialize  $\mathbf{X}_i^{\tilde{r}}$  as an empty array
3 Initialize  $\mathbf{M}_i$  as an empty array
4 for  $j = 1$  to  $T$  do
5   if  $j = 1$  then
6      $\mathbf{X}_i^{\tilde{r}}(t_0), \mathbf{M}_i(t_0), \{\theta^{(c)}, \theta^{(m)}, \theta^{(b)}, \dots\} \leftarrow$ 
       SBI( $\mathbf{X}_i^r(t_0), \mathbf{l}_i(t_0)$ )
7      $\mathbf{X}_i^{\tilde{r}} \leftarrow \mathbf{X}_i^{\tilde{r}} \cup \{\mathbf{X}_i^{\tilde{r}}(t_0)\}$ 
8      $\mathbf{M}_i \leftarrow \mathbf{M}_i \cup \{\mathbf{M}_i(t_0)\}$ 
9      $\theta^{(sbi)} \leftarrow \{\theta^{(c)}, \theta^{(m)}, \theta^{(b)}, \dots\}$ 
10  end
11  else
12     $\mathbf{l}_i(t) \leftarrow \text{LandmarkInterpolation}(\mathbf{l}_i(t),$ 
       $\mathbf{l}_i(t-1), \bar{d}, \tau)$ 
13     $\mathbf{X}_i^{\tilde{r}}(t), \mathbf{M}_i(t), \_ \leftarrow \text{SBI}(\mathbf{X}_i^r(t), \mathbf{l}_i(t), \theta^{(sbi)})$ 
14     $\mathbf{X}_i^{\tilde{r}} \leftarrow \mathbf{X}_i^{\tilde{r}} \cup \{\mathbf{X}_i^{\tilde{r}}(t)\}$ 
15     $\mathbf{M}_i \leftarrow \mathbf{M}_i \cup \{\mathbf{M}_i(t)\}$ 
16  end
17 end
18 return  $\mathbf{X}_i^{\tilde{r}}, \mathbf{M}_i$ 

```

mark Interpolation module (Section 3.1 in the main paper) in generating high-quality pseudo-fake videos, we show some SBV samples, their blending boundaries, original landmarks, and those modified by the proposed modules in Figure 7. In the top part of the figure, we compare data generated using only CSP to data generated with both CSP and the Landmark Interpolation module. We observe that the Landmark Interpolation module ensures smooth transitions of facial landmarks between consecutive frames ($t \rightarrow t+1$). In the bottom part of the figure, we compare data generated with only CSP to data generated without any of the proposed SBVs components. We observe significant variations in the manipulated facial areas when CSP is omitted. Therefore, the proposed CSP and Landmark Interpolation module effectively enhance the temporal coherence of the generated SBVs.

6.4. Impact of SBVs

To verify the advantage of using SBVs for improving the generalization of detectors, we conduct several experiments using different binary classifiers trained either with SBVs or with one of the four types of forgeries forming FF++ [45] (DF [10], F2F [50], FS [30], NT [49]). For a



Figure 7. **Illustration of the facial landmarks, the generated SBV, and the blending boundary** with and without applying the Consistent Synthesized Parameters (CSP) module and the Landmark Interpolation module.

fair comparison, a widely-used CNN-based Resnet3D [26] and a Transformer-based TimeSformer [2] are employed. We note that both selected models are trained from *Scratch* (S) without pretrained initialization. Table. 9 presents the generalization performance in terms of AUC (%) on five datasets [13, 14, 16, 35, 68] respectively when trained with different manipulation methods from FF+. Notably, training with SBVs significantly increases the overall generalizability capability of binary models as compared to those trained on using one specific manipulation. This indicates the importance of highly realistic, naturally consistent generated pseudo-fake videos.

6.5. Robustness to Unseen Perturbations

In the main manuscript, we report in Figure. 5 the “Average” performance under different corruptions. This section complements this experiment by reporting the mean performance across different severity levels for each degradation type, as detailed in Table. 10. Except for a slight decrease in

effectiveness under “Color Saturation” compared to LAA-Net [42], FakeSTormer is generally more robust to the unseen perturbations as compared to other augmented-based methods [32, 34, 42, 47].

6.6. Multi-shot Inferences

Models can sometimes be overconfident in their predictions, which negatively impacts the generalizability aspect [40, 61]. To address this issue, we explore the possibility of regularizing the input during testing. Specifically, we propose multi-shot inference, leveraging Vulnerability-Driven Cutout Augmentation by utilizing the temporal head output \hat{D} . We use \hat{D} because the most significant temporal changes in vulnerable areas over time, from $t \rightarrow (t + 1)$, are likely to occur at the spatial locations corresponding to the highest values of \hat{B} (Eq.3 in the main manuscript).

In particular, given a test video, after the first shot of inference, the prediction map \hat{D} can be leveraged to generate a new masked video through the proposed Cutout augmen-

| Method | Training set | | | | | Test set AUC (%) | | | | | | Avg. |
|------------------------|--------------|----|----|-----|----|------------------|-------------|-------------|-------------|-------------|-------------|--------------------|
| | Real | DF | FS | F2F | NT | FF++ | CDF2 | DFD | DFDCP | DFDC | DFW | |
| ResNet3D [26] | ✓ | ✓ | × | × | × | 72.5 | 58.5 | 51.3 | 53.4 | 59.4 | 65.0 | 60.0 |
| TimeSFormer [2] | ✓ | ✓ | × | × | × | 65.4 | 59.3 | 66.1 | 53.5 | 61.4 | 57.5 | 60.5 |
| ResNet3D [26] | ✓ | × | ✓ | × | × | 70.6 | 61.1 | 50.6 | 59.2 | 55.8 | 51.5 | 58.1 |
| TimeSFormer [2] | ✓ | × | ✓ | × | × | 76.4 | 51.7 | 43.7 | 44.6 | 54.5 | 43.9 | 52.5 |
| ResNet3D [26] | ✓ | × | × | ✓ | × | 78.0 | 63.8 | 54.5 | 63.4 | 55.7 | 50.1 | 60.9 |
| TimeSFormer [2] | ✓ | × | × | ✓ | × | 81.1 | 64.4 | 60.1 | 64.5 | 52.0 | 50.5 | 62.1 |
| ResNet3D [26] | ✓ | × | × | × | ✓ | 72.7 | 63.7 | 75.6 | 69.1 | 59.6 | 62.6 | 67.2 |
| TimeSFormer [2] | ✓ | × | × | × | ✓ | 75.5 | 65.8 | 84.7 | 70.3 | 62.7 | 65.5 | 70.8 |
| ResNet3D [26] + SBVs | ✓ | × | × | × | × | 90.2 | 85.9 | 85.0 | 82.8 | 66.4 | 67.5 | 79.6(↑12.4) |
| TimeSFormer [2] + SBVs | ✓ | × | × | × | × | 94.7 | 89.5 | 95.6 | 88.6 | 72.5 | 70.9 | 85.3(↑14.5) |

Table 9. **Cross-dataset generalization.** Performance comparison in terms of AUC (%) on multiple datasets of different binary classification models [2, 26] trained using our video synthesis (SBVs) and normal fake data [45]. All models are trained on FF++(c23) [45] from *Scratch* (S) and are tested on other datasets [13, 14, 16, 35, 68]. Gray indicates the use of normal fake data for training. **Bold** and underline highlight the best and the second-best performance, respectively.

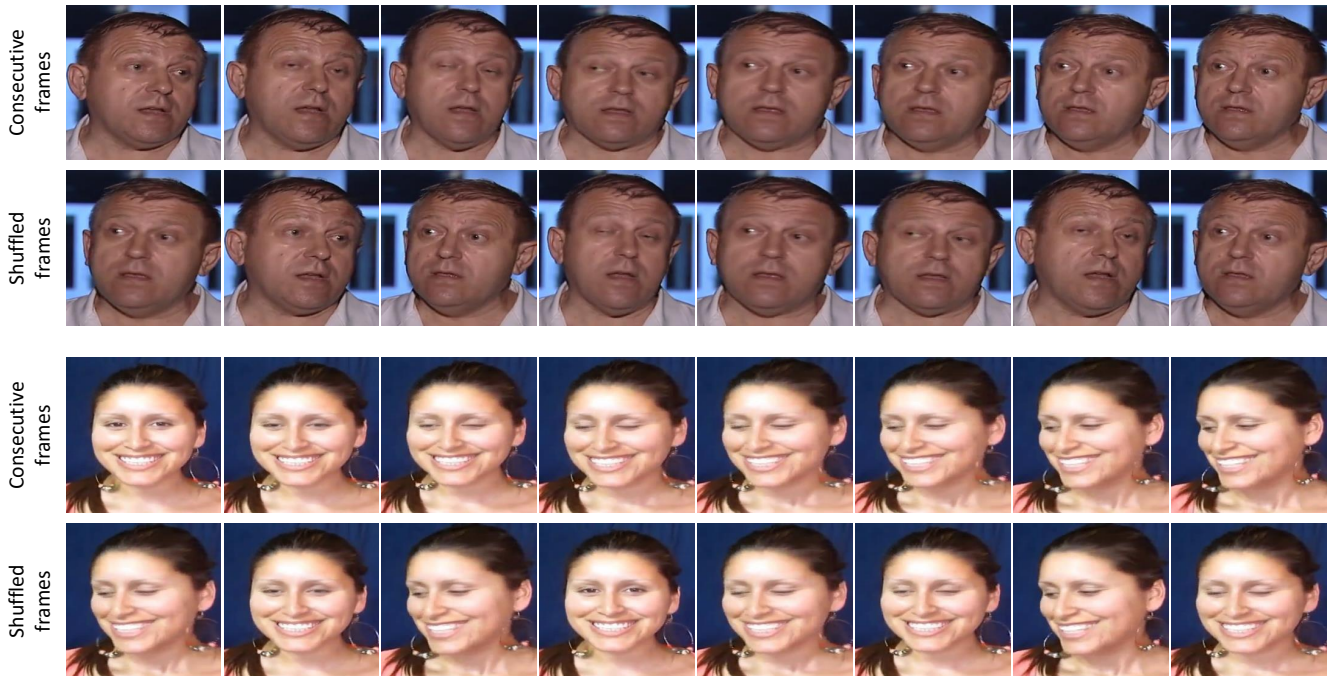


Figure 8. **Shuffled frames can produce obvious temporal inconsistencies.**

tation for the second inference shot. Specifically, we select $\tilde{\mathbf{D}}$ at $t = 2$ (capturing the temporal transition from the first \rightarrow the second frame) to define the set \mathcal{P} (Section 3.1 of the main manuscript) for determining Cutout positions. This iterative process can be repeated for multiple inference shots.

Table 11 presents the cross-evaluation results with five shots of inference on five unseen datasets [13, 14, 16, 35, 68] using the model trained on FF++ [45]. The results indicate a gradual improvement in generalization performance after each iteration. This suggests that the prediction outputs are not only interpretable but also can be used potentially to enhance the model performance.

6.7. Visualization of Saliency Maps

To analyze the contribution of the two proposed branches h and g in the detection performance of FakeSTormer, we visualize the input regions activated by those branches. For that purpose, we adopt Grad-CAM [46] for the temporal branch h and utilize the final SA scores of spatial tokens for the spatial branch g . The visualization results from various datasets are presented in Figure 9. It can be observed that FakeSTormer can discriminate between real and fake videos by focusing on very few, different local areas, even without having seen those types of forgeries during training.

| Method | Fake | Contrast | Saturation | Gaussian Blur | Gaussian Noise | JPEG Compression | Block Wise | Avg |
|---------------|------|-------------|-------------|---------------|----------------|------------------|-------------|-------------|
| DSP-FWA [34] | ✓ | 80.7 | 79.6 | 67.3 | 61.8 | 68.0 | 76.6 | 72.3 |
| FaceXray [32] | ✓ | 88.9 | 96.0 | 70.0 | 58.0 | 62.2 | 94.7 | 78.3 |
| SBI [47] | | 92.3 | 92.0 | 72.7 | <u>62.2</u> | <u>79.1</u> | 92.2 | 81.7 |
| LAA-Net [42] | | <u>95.0</u> | 97.0 | <u>73.2</u> | 57.5 | 75.2 | <u>94.9</u> | <u>82.1</u> |
| Ours | | 97.6 | 96.3 | 81.6 | 65.4 | 92.9 | 96.8 | 88.4 |

Table 10. **Robustness to unseen perturbations.** Average AUC scores (%) across all levels for each degradation type.

| No. shots | Test set AUC (%) | | | | | Avg. |
|-----------|------------------|--------------|--------------|--------------|--------------|----------------------|
| | CDF2 | DFD | DFDCP | DFDC | DFW | |
| 1 | 92.35 | 98.47 | 90.02 | 74.56 | 74.19 | 85.92 |
| 2 | 92.34 | <u>98.51</u> | <u>90.11</u> | <u>74.60</u> | 74.25 | 85.96(†0.04) |
| 3 | 92.38 | 98.52 | 90.13 | 74.61 | <u>74.28</u> | 85.98(†0.06) |
| 4 | 92.38 | 98.52 | 90.13 | 74.61 | 74.30 | 85.99(†0.07) |
| 5 | <u>92.36</u> | 98.52 | 90.13 | 74.61 | 74.30 | <u>85.98</u> (†0.06) |

Table 11. **Multi-shot inferences.** AUC (%) comparison of our model using different numbers of shots in the cross-dataset setup. The AUC slightly increases with a higher number of shots.

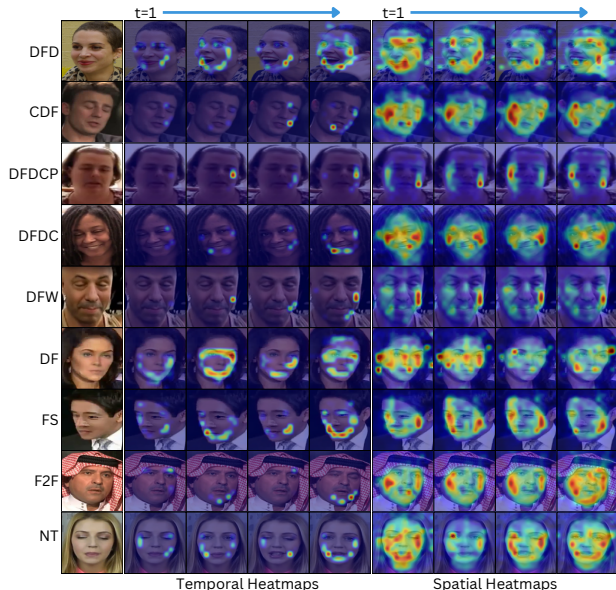


Figure 9. **Visualization of Saliency Maps.** The second-fifth and sixth-ninth columns represent temporal heatmaps and spatial heatmaps on different frames in the video, respectively. All datasets are unseen during validation.

6.8. STG [33]: Shuffled Frames can produce obvious Temporal Inconsistencies

We propose SBVs to generate subtler artifacts for pseudo-fakes compared to the STG approach used in [33]. We believe that STG may produce obvious (low-quality) temporal artifacts, as it shuffles frames in the temporal domain, leading to significant inconsistencies. Figure 8 illustrates how shuffling creates noticeable discrepancies between frames. In contrast, our SBVs leverage consecutive

frames to produce subtler temporal artifacts while simulating these artifacts in a different manner (as detailed in Section 3.1 of the main manuscript).

6.9. Details on the Datasets

Datasets. For our experiments, we select datasets that haven’t typically used as benchmarks in previous works [3, 9, 54–56, 58, 62, 65]. For both training and validation, we employ **FaceForensics++** (FF++) [45], which consists of 1,000 real videos and 4,000 fake videos generated using four manipulation methods: (Deepfakes (DF) [10], FaceSwap (FS) [30], Face2Face (F2F) [50], and Neural-Textures (NT) [49]). It can be noted that, for training, we use only the real videos and generate pseudo-fake data using our synthesized method, SBVs. By default, the c23 version of FF++ is adopted, following the recent literature [9, 55, 56, 62, 65].

For further validation, we also evaluate on the following datasets: (1) **Celeb-DFv2** (CDF) [35], a well-known benchmark with high-quality deepfakes; (2) **DeepfakeDetection** (DFD) [16], which includes 3,000 forged videos featuring 28 actors in various scenes; (3) **Deepfake Detection Challenge Preview** (DFDCP) [13] and (4) **Deepfake Detection Challenge** (DFDC) [14], a large-scale dataset containing numerous distorted videos with issues such as compression and noise; and (5) **WildDeepfake** (DFW) [68], a dataset fully sourced from the internet, without prior knowledge of manipulation methods.

Data Pre-processing. Following the splitting convention [45], we extract 256, 32, and 32 consecutive frames for training, validation, and testing, respectively. Facial regions are cropped using Face-RetinaNet [11]. These bounding boxes are conservatively enlarged by a factor of 1.25 around the center of the face and then resized to a fixed resolution of 224×224 . Additionally, we store 81 facial landmarks for each frame, extracted using Dlib [29]. Finally, the preserved landmark keypoints are utilized to dynamically generate pseudo-fakes during each training iteration.

6.10. Revisited TimeSformer: Implementation Details

We choose TimeSformer [2] as our feature extractor given its ability to effectively capture separate long-range temporal information and spatial features. First, given a video $\mathbf{X} \in \mathbb{R}^{C \times T \times H \times W}$, its frames in each time step

are split into N number of non-overlapping patches of size $P \times P$, i.e., $N = \frac{H \times W}{P^2}$. Each patch is flattened as $\mathbf{x}_{(t,p)} \in \mathbb{R}^{C \cdot P^2}$, and is then linearly mapped into D -dimensional embedding vector $\mathbf{z}_{(t,p)}^0 \in \mathbb{R}^D$ by means of a learnable matrix $E \in \mathbb{R}^{D \times C \cdot P^2}$ where $t = [[1, T]]$ indexes temporal positions, and $p = [[1, N]]$ indexes spatial positions. The process results in an input patch embedding matrix $\mathbf{Z}^0 \in \mathbb{R}^{T \times N \times D}$.

In TimeSformer, a global class token \mathbf{z}_{cls} attends to all patches and then is used for classification. This mechanism implicitly captures mixed spatial-temporal features at the same time, which might lead to overfitting on a specific type of domain artifacts [55, 65]. We revisit it slightly in order to decouple the spatial and temporal information by considering two sorts of additional tokens (one spatial and one temporal).

For that purpose, we attach in each dimension of \mathbf{Z}^0 , a spatial token $\mathbf{z}_s^0 \in \mathbb{R}^D$ and a temporal token $\mathbf{z}_t^0 \in \mathbb{R}^D$, respectively. These tokens will independently interact only with patch embeddings belonging to their dimension axis by leveraging the decomposed SA [2]. This mechanism not only facilitates the disentanglement learning process of spatio-temporal features but is also beneficial to optimize the computational complexity of $\mathcal{O}(T^2 + N^2)$ as compared to $\mathcal{O}(T^2 \cdot N^2)$ in vanilla SA. Those tokens will be then fed into L ($L = 12$ as default) transformer encoder blocks in which each block contains a multi-head temporal SA (TSA), a multi-head spatial SA (SSA), LayerNorm (LN), and a multi-layer perception (MLP). Note that, for the sake of matrix compatibility, a placeholder embedding $\mathbf{z}_{(0,0)}^0$ is attached. Formally, the feature extraction process can be summarized as follows,

$$[\mathbf{Z}^L, \mathbf{z}_s^L, \mathbf{z}_t^L] = \Phi(\mathbf{X}), \quad (15)$$

where \mathbf{Z}^L is the final patch embedding matrix, \mathbf{z}_s^L the resulting set of spatial tokens, and \mathbf{z}_t^L the resulting set of temporal tokens that will be respectively sent to the temporal head h , the spatial head g , and the classification head f . Our overall framework is illustrated in Figure. 2 of the main paper.

References

- [1] Yuval Alaluf, Or Patashnik, Zongze Wu, Asif Zamir, Eli Shechtman, Dani Lischinski, and Daniel Cohen-Or. Third time’s the charm? image and video editing with stylegan3. *CoRR*, abs/2201.13433, 2022. 1
- [2] Gedas Bertasius, Heng Wang, and Lorenzo Torresani. Is space-time attention all you need for video understanding? In *Proceedings of the International Conference on Machine Learning (ICML)*, 2021. 2, 5, 6, 7, 10, 11, 12, 13
- [3] Junyi Cao, Chao Ma, Taiping Yao, Shen Chen, Shouhong Ding, and Xiaokang Yang. End-to-end reconstruction-classification learning for face forgery detection. In *2022 IEEE/CVF Conference on Computer Vision and Pattern Recognition (CVPR)*, pages 4103–4112, 2022. 1, 6, 7, 12
- [4] Mathilde Caron, Hugo Touvron, Ishan Misra, Hervé Jégou, Julien Mairal, Piotr Bojanowski, and Armand Joulin. Emerging properties in self-supervised vision transformers. *CoRR*, abs/2104.14294, 2021. 6
- [5] Heather Chen and Kathleen Magramo. Finance worker pays out \$25 million after video call with deepfake ”chief financial officer”. <https://edition.cnn.com/2024/02/04/asia/deepfake-cfo-scam-hong-kong-intl-hnk/index.html>, 2024. [Online; accessed 4-February-2024]. 1
- [6] Liang Chen, Yong Zhang, Yibing Song, Lingqiao Liu, and Jue Wang. Self-supervised learning of adversarial example: Towards good generalizations for deepfake detection. In *Proceedings of the IEEE/CVF Conference on Computer Vision and Pattern Recognition (CVPR)*, pages 18710–18719, 2022. 1, 2, 3, 6, 7
- [7] Liang Chen, Yong Zhang, Yibing Song, Jue Wang, and Lingqiao Liu. Ost: Improving generalization of deepfake detection via one-shot test-time training. In *Advances in Neural Information Processing Systems*, pages 24597–24610. Curran Associates, Inc., 2022. 1, 3
- [8] Juhwan Choi and YoungBin Kim. Colorful cutout: Enhancing image data augmentation with curriculum learning, 2024. 4
- [9] Jongwook Choi, Taehoon Kim, Yonghyun Jeong, Seungryul Baek, and Jongwon Choi. Exploiting style latent flows for generalizing deepfake video detection. In *Proceedings of the IEEE/CVF Conference on Computer Vision and Pattern Recognition (CVPR)*, pages 1133–1143, 2024. 3, 6, 7, 12
- [10] Deepfakes. Faceswapdevs. <https://github.com/deepfakes/faceswap>, 2019. 6, 9, 12
- [11] Jiankang Deng, Jia Guo, Yuxiang Zhou, Jinke Yu, Irene Kotisia, and Stefanos Zafeiriou. Retinaface: Single-stage dense face localisation in the wild. *CoRR*, abs/1905.00641, 2019. 7, 12
- [12] Terrance DeVries and Graham W. Taylor. Improved regularization of convolutional neural networks with cutout, 2017. 4
- [13] Brian Dolhansky, Russ Howes, Ben Pflaum, Nicole Baram, and Cristian Canton-Ferrer. The deepfake detection challenge (DFDC) preview dataset. *CoRR*, abs/1910.08854, 2019. 6, 7, 9, 10, 11, 12
- [14] Brian Dolhansky, Joanna Bitton, Ben Pflaum, Jikuo Lu, Russ Howes, Menglin Wang, and Cristian Canton-Ferrer. The deepfake detection challenge dataset. *CoRR*, abs/2006.07397, 2020. 6, 7, 9, 10, 11, 12
- [15] Shichao Dong, Jin Wang, Renhe Ji, Jiajun Liang, Haoqiang Fan, and Zheng Ge. Implicit identity leakage: The stumbling block to improving deepfake detection generalization. In *Proceedings of the IEEE/CVF Conference on Computer Vision and Pattern Recognition (CVPR)*, pages 3994–4004, 2023. 1, 3
- [16] Nick Dufour and Andrew Gully. Contributing data to deepfake detection research. <https://ai.googleblog.com/2019/09/contributing->

- [data-to-deepfake-detection.html](#), 2019. 6, 7, 9, 10, 11, 12
- [17] Pierre Foret, Ariel Kleiner, Hossein Mobahi, and Behnam Neyshabur. Sharpness-aware minimization for efficiently improving generalization. *CoRR*, abs/2010.01412, 2020. 7
- [18] Niki Maria Foteinopoulou, Enjie Ghorbel, and Djamila Aouada. A hitchhikers guide to fine-grained face forgery detection using common sense reasoning. *arXiv preprint arXiv:2410.00485*, 2024. 2
- [19] Tsu-Jui Fu, Xin Eric Wang, Scott T. Grafton, Miguel P. Eckstein, and William Yang Wang. M3l: Language-based video editing via multi-modal multi-level transformers. In *Proceedings of the IEEE/CVF Conference on Computer Vision and Pattern Recognition (CVPR)*, pages 10513–10522, 2022. 1
- [20] Ipek Ganiyusufoglu, L. Minh Ngô, Nedko Savov, Sezer Karaoglu, and Theo Gevers. Spatio-temporal features for generalized detection of deepfake videos. *CoRR*, abs/2010.11844, 2020. 1, 3
- [21] Chengyue Gong, Dilin Wang, Meng Li, Vikas Chandra, and Qiang Liu. Keepaugment: A simple information-preserving data augmentation approach. In *Proceedings of the IEEE/CVF conference on computer vision and pattern recognition*, pages 1055–1064, 2021. 4
- [22] Zhihao Gu, Yang Chen, Taiping Yao, Shouhong Ding, Jilin Li, Feiyue Huang, and Lizhuang Ma. Spatiotemporal inconsistency learning for deepfake video detection. *Proceedings of the 29th ACM International Conference on Multimedia*, 2021. 1, 3, 6
- [23] Weinan Guan, Wei Wang, Bo Peng, Jing Dong, and Tieniu Tan. St-sbv: Spatial-temporal self-blended videos for deepfake detection. In *Chinese Conference on Pattern Recognition and Computer Vision (PRCV)*, pages 274–288. Springer, 2024. 6
- [24] Alexandros Haliassos, Konstantinos Vougioukas, Stavros Petridis, and Maja Pantic. Lips don't lie: A generalisable and robust approach to face forgery detection. *CoRR*, abs/2012.07657, 2020. 1, 2, 3, 6, 7
- [25] Alexandros Haliassos, Rodrigo Mira, Stavros Petridis, and Maja Pantic. Leveraging real talking faces via self-supervision for robust forgery detection. In *Proceedings of the IEEE/CVF Conference on Computer Vision and Pattern Recognition (CVPR)*, pages 14950–14962, 2022. 6, 7
- [26] Kensho Hara, Hirokatsu Kataoka, and Yutaka Satoh. Can spatiotemporal 3d cnns retrace the history of 2d cnns and imagenet? In *Proceedings of the IEEE Conference on Computer Vision and Pattern Recognition (CVPR)*, pages 6546–6555, 2018. 6, 7, 10, 11
- [27] Kaiming He, Xinlei Chen, Saining Xie, Yanghao Li, Piotr Dollár, and Ross Girshick. Masked autoencoders are scalable vision learners. In *Proceedings of the IEEE/CVF Conference on Computer Vision and Pattern Recognition (CVPR)*, pages 16000–16009, 2022. 7
- [28] Liming Jiang, Ren Li, Wayne Wu, Chen Qian, and Chen Change Loy. DeeperForensics-1.0: A large-scale dataset for real-world face forgery detection. In *CVPR*, 2020. 7, 8
- [29] Davis E. King. Dlib-ml: A machine learning toolkit. *J. Mach. Learn. Res.*, 10:1755–1758, 2009. 7, 12
- [30] Marek Kowalski. Faceswap. <https://github.com/MarekKowalski/FaceSwap>, 2018. 6, 9, 12
- [31] Lingzhi Li, Jianmin Bao, Hao Yang, Dong Chen, and Fang Wen. Advancing high fidelity identity swapping for forgery detection. In *2020 IEEE/CVF Conference on Computer Vision and Pattern Recognition (CVPR)*, pages 5073–5082, 2020. 1
- [32] Lingzhi Li, Jianmin Bao, Ting Zhang, Hao Yang, Dong Chen, Fang Wen, and Baining Guo. Face x-ray for more general face forgery detection. In *IEEE/CVF Conference on Computer Vision and Pattern Recognition (CVPR)*, 2020. 1, 2, 3, 4, 6, 7, 10, 12
- [33] Maosen Li, Xurong Li, Kun Yu, Cheng Deng, Heng Huang, Feng Mao, Hui Xue, and Minghao Li. Spatio-temporal catcher: A self-supervised transformer for deepfake video detection. In *Proceedings of the 31st ACM International Conference on Multimedia*, pages 8707–8718, 2023. 2, 3, 6, 12
- [34] Yuezun Li and Siwei Lyu. Exposing deepfake videos by detecting face warping artifacts. In *IEEE Conference on Computer Vision and Pattern Recognition Workshops (CVPRW)*, 2019. 7, 10, 12
- [35] Yuezun Li, Xin Yang, Pu Sun, Honggang Qi, and Siwei Lyu. Celeb-df: A large-scale challenging dataset for deepfake forensics. In *IEEE/CVF Conference on Computer Vision and Pattern Recognition (CVPR)*, 2020. 6, 7, 9, 10, 11, 12
- [36] Yuchen Luo, Yong Zhang, Junchi Yan, and Wei Liu. Generalizing face forgery detection with high-frequency features. In *Proceedings of the IEEE/CVF Conference on Computer Vision and Pattern Recognition (CVPR)*, pages 16317–16326, 2021. 6
- [37] Qingxuan Lv, Yuezun Li, Junyu Dong, Sheng Chen, Hui Yu, Huiyu Zhou, and Shu Zhang. Domainforensics: Exposing face forgery across domains via bi-directional adaptation. *IEEE Transactions on Information Forensics and Security*, 19:7275–7289, 2024. 6, 7
- [38] Ghazal Mazaheri and Amit K Roy-Chowdhury. Detection and localization of facial expression manipulations. In *Proceedings of the IEEE/CVF Winter Conference on Applications of Computer Vision*, pages 1035–1045, 2022. 2
- [39] Nesryne Mejri, Enjie Ghorbel, and Djamila Aouada. Untag: Learning generic features for unsupervised type-agnostic deepfake detection. In *ICASSP 2023 - 2023 IEEE International Conference on Acoustics, Speech and Signal Processing (ICASSP)*, pages 1–5, 2023. 1, 2, 3
- [40] Rafael Müller, Simon Kornblith, and Geoffrey E. Hinton. When does label smoothing help? *CoRR*, abs/1906.02629, 2019. 6, 10
- [41] Dat Nguyen, Marcella Astrid, Enjie Ghorbel, and Djamila Aouada. Fakeformer: Efficient vulnerability-driven transformers for generalisable deepfake detection, 2024. 1, 2, 3, 4, 5, 9
- [42] Dat Nguyen, Nesryne Mejri, Inder Pal Singh, Polina Kuleshova, Marcella Astrid, Anis Kacem, Enjie Ghorbel,

- and Djamilia Aouada. Laa-net: Localized artifact attention network for quality-agnostic and generalizable deepfake detection. In *Proceedings of the IEEE/CVF Conference on Computer Vision and Pattern Recognition (CVPR)*, pages 17395–17405, 2024. 1, 2, 3, 4, 5, 6, 7, 10, 12
- [43] Yuyang Qian, Guojun Yin, Lu Sheng, Zixuan Chen, and Jing Shao. Thinking in frequency: Face forgery detection by mining frequency-aware clues. In *European conference on computer vision*, pages 86–103. Springer, 2020. 6
- [44] Reuters. South korea to criminalize watching or possessing sexually explicit deepfakes. <https://edition.cnn.com/2024/09/26/asia/south-korea-deepfake-bill-passed-intl-hnk/index.html>, 2024. [Online; accessed 26-September-2024]. 1
- [45] Andreas Rössler, Davide Cozzolino, Luisa Verdoliva, Christian Riess, Justus Thies, and Matthias Nießner. FaceForensics++: Learning to detect manipulated facial images. In *International Conference on Computer Vision (ICCV)*, 2019. 1, 6, 7, 8, 9, 11, 12
- [46] Ramprasaath R. Selvaraju, Abhishek Das, Ramakrishna Vedantam, Michael Cogswell, Devi Parikh, and Dhruv Batra. Grad-cam: Why did you say that? visual explanations from deep networks via gradient-based localization. *CoRR*, abs/1610.02391, 2016. 11
- [47] Kaede Shiohara and Toshihiko Yamasaki. Detecting deepfakes with self-blended images. In *Proceedings of the IEEE/CVF Conference on Computer Vision and Pattern Recognition*, pages 18720–18729, 2022. 1, 2, 3, 4, 6, 7, 8, 10, 12
- [48] Guocong Song and Wei Chai. Collaborative learning for deep neural networks. In *Neural Information Processing Systems*, 2018. 6
- [49] Justus Thies, Michael Zollhöfer, and Matthias Nießner. Deferred neural rendering: Image synthesis using neural textures. *CoRR*, abs/1904.12356, 2019. 6, 9, 12
- [50] Justus Thies, Michael Zollhöfer, Marc Stamminger, Christian Theobalt, and Matthias Nießner. Face2face: Real-time face capture and reenactment of RGB videos. *CoRR*, abs/2007.14808, 2020. 1, 6, 9, 12
- [51] Hugo Touvron, Matthieu Cord, Matthijs Douze, Francisco Massa, Alexandre Sablayrolles, and Hervé Jégou. Training data-efficient image transformers & distillation through attention. *CoRR*, abs/2012.12877, 2020. 6
- [52] Jane Wakefield. Deepfake presidents used in Russia-Ukraine war. <https://www.bbc.com/news/technology-60780142>, 2022. [Online; accessed 7-March-2023]. 1
- [53] Chengrui Wang and Weihong Deng. Representative forgery mining for fake face detection. In *IEEE Conference on Computer Vision and Pattern Recognition (CVPR)*, 2021. 4, 6
- [54] Yuan Wang, Kun Yu, Chen Chen, Xiyuan Hu, and Silong Peng. Dynamic graph learning with content-guided spatial-frequency relation reasoning for deepfake detection. In *Proceedings of the IEEE/CVF Conference on Computer Vision and Pattern Recognition (CVPR)*, pages 7278–7287, 2023. 6, 7, 12
- [55] Zhendong Wang, Jianmin Bao, Wengang Zhou, Weilun Wang, and Houqiang Li. Altfreezing for more general video face forgery detection. In *Proceedings of the IEEE/CVF Conference on Computer Vision and Pattern Recognition (CVPR)*, pages 4129–4138, 2023. 1, 2, 3, 6, 7, 12, 13
- [56] Yuting Xu, Jian Liang, Gengyun Jia, Ziming Yang, Yanhao Zhang, and Ran He. Tall: Thumbnail layout for deepfake video detection. In *Proceedings of the IEEE/CVF International Conference on Computer Vision (ICCV)*, pages 22658–22668, 2023. 1, 3, 6, 7, 12
- [57] Zhiliang Xu, Zhibin Hong, Changxing Ding, Zhen Zhu, Junyu Han, Jingtuo Liu, and Errui Ding. Mobilefaceswap: A lightweight framework for video face swapping. In *Proceedings of the AAAI Conference on Artificial Intelligence*, 2022. 1
- [58] Zhiyuan Yan, Yong Zhang, Yanbo Fan, and Baoyuan Wu. Ucf: Uncovering common features for generalizable deepfake detection. In *Proceedings of the IEEE/CVF International Conference on Computer Vision (ICCV)*, pages 22412–22423, 2023. 6, 12
- [59] Zhiyuan Yan, Yuhao Luo, Siwei Lyu, Qingshan Liu, and Baoyuan Wu. Transcending forgery specificity with latent space augmentation for generalizable deepfake detection. In *Proceedings of the IEEE/CVF Conference on Computer Vision and Pattern Recognition (CVPR)*, pages 8984–8994, 2024. 6
- [60] Daichi Zhang, Fanzhao Lin, Yingying Hua, Pengju Wang, Dan Zeng, and Shiming Ge. Deepfake video detection with spatiotemporal dropout transformer. In *Proceedings of the 30th ACM international conference on multimedia*, pages 5833–5841, 2022. 1, 2, 3
- [61] Hongyi Zhang, Moustapha Cissé, Yann N. Dauphin, and David Lopez-Paz. mixup: Beyond empirical risk minimization. *CoRR*, abs/1710.09412, 2017. 6, 10
- [62] Cairong Zhao, Chutian Wang, Guosheng Hu, Haonan Chen, Chun Liu, and Jinhui Tang. Istvt: Interpretable spatial-temporal video transformer for deepfake detection. *IEEE Transactions on Information Forensics and Security*, 18: 1335–1348, 2023. 1, 2, 3, 6, 7, 12
- [63] Eric Zhao, Xiang Xu, Mingze Xu, Hui Ding, Yuanjun Xiong, and Wei Xia. Learning self-consistency for deepfake detection. In *ICCV 2021*, 2021. 2, 3, 6
- [64] Hanqing Zhao, Wenbo Zhou, Dongdong Chen, Tianyi Wei, Weiming Zhang, and Nenghai Yu. Multi-attentional deepfake detection. In *Proceedings of the IEEE/CVF conference on computer vision and pattern recognition*, pages 2185–2194, 2021. 1, 6
- [65] Yinglin Zheng, Jianmin Bao, Dong Chen, Ming Zeng, and Fang Wen. Exploring temporal coherence for more general video face forgery detection. In *Proceedings of the IEEE/CVF International Conference on Computer Vision (ICCV)*, pages 15044–15054, 2021. 1, 2, 3, 5, 6, 7, 12, 13
- [66] Zhun Zhong, Liang Zheng, Guoliang Kang, Shaozi Li, and Yi Yang. Random erasing data augmentation. *CoRR*, abs/1708.04896, 2017. 4
- [67] Yuhao Zhu, Qi Li, Jian Wang, Chengzhong Xu, and Zhenan Sun. One shot face swapping on megapixels. In *Proceedings of the IEEE conference on computer vision and pattern recognition (CVPR)*, pages 4834–4844, 2021. 1

- [68] Bojia Zi, Minghao Chang, Jingjing Chen, Xingjun Ma, and Yu-Gang Jiang. Wildeepfake: A challenging real-world dataset for deepfake detection. *Proceedings of the 28th ACM International Conference on Multimedia*, 2020. [6](#), [7](#), [9](#), [10](#), [11](#), [12](#)